Supporting Information for

Plasmonic Electronic Raman Scattering as Internal Standard for Spatial and Temporal Calibration in Quantitative Surface-enhanced Raman Spectroscopy

*Wonil Nam[1], Yuming Zhao[1], Junyeob Song[1,2], Seied Ali Safiabadi Tali[1], Seju Kang[3], Wenqi Zhu[2], Henri J. Lezec[2], Amit Agrawal[2, 4], Peter J. Vikesland[3], and Wei Zhou[1,]***

[1]Department of Electrical and Computer Engineering, Virginia Tech, Blacksburg, Virginia 24061, USA

[2]Physical Measurement Laboratory, National Institute of Standards and Technology, Gaithersburg, Maryland 20899, USA

[3]Department of Civil and Environmental Engineering, Institute of Critical Technology and Applied Science Sustainable Nanotechnology Center, Virginia Tech, Blacksburg, Virginia, 24061, USA

[4]Institute for Research in Electronics and Applied Physics and Maryland NanoCenter, University of Maryland, College Park, Maryland 20742, USA

**email:* wzh@vt.edu

Theoretical analysis of SERS calibration by ERS signals

Figure 1A-left shows an energy-diagram illustration of the ERS process in plasmonic nanostructures. For Au at room temperature, most electronic states in *sp*-bands are occupied below the Fermi energy (E_F) following the Fermi-Dirac distribution.[1] In the ERS process, an electron in the conduction band close to the Fermi level can be optically excited to a virtual state and instantaneously relax to another state in the conduction band with slightly different energy and momentum following the *E*-*k* dispersion relation of *sp*-bands.[2-4] By using a near-infrared (NIR) laser excitation (785 nm) with photon energy far below the interband transition energy of Au, one can avoid the interband transitions induced photoluminescence in the SERS background. The plasmonic ERS intensity is proportional to the density of electron-hole pairs, n_{e-h}, in metal nanostructures[2-4] expressed as $n_{e-h}(\Delta\omega_e) = \left|exp\left(-\frac{\hbar\Delta\omega_e}{k_BT}\right) - 1\right|^{-1}$ where $\Delta\omega_e$ is the Stokes-shifted frequency for the ERS process, $\hbar$ is the Planck's constant, k_B is the Boltzmann constant, and T is the temperature. Therefore, the ERS intensity exponentially increases when $\Delta\omega_e$ approaches zero. Under the continuous-wave (CW) laser excitation with low powers (< 1 mW), the conduction-band electrons and lattice photons in metal nanostructures can reach thermal equilibrium to have nearly the same temperature through fast relaxation of photo-excited hot electrons. At the low-wavenumber range of energy shifts, ERS signals can dominate the SERS emission background by NIR laser excitation in Au nanostructures since intraband transition photoluminescence additionally requires significant momentum Δk to match the *sp*-band electron dispersion (Figure 1A-left).[3,4] Compelling evidence has recently confirmed this case under the right condition, although it is still insufficient to explain light emission from plasmonic nanostructures under ultrafast pulsed laser excitation.[5-7] In the ultrafast regime, where the pulse-width of lasers is compressed to an ultrashort timescale such as pico- or femto- second comparable

or shorter than the electron-phonon scattering lifetime, both theoretical and experimental studies show that the energy of the photoexcited hot electrons are accumulated in the temporal domain, and thus the electrons form a Fermi-Dirac distribution with a much higher temperature (thousands of *K*) than the lattice.[5, 7-10]

For the case of excitation with NIR CW, by using a long-pass filter to block the laser line (Rayleigh scattering), the filtered ERS background continuum exhibits an ERS pseudo-peak with signal intensity $I_{\mathrm{ERS}}(\omega_o - \Delta\omega_e)$ in the measured Raman spectra (Figure 1A-right), where ω_o is the laser excitation frequency. Similar to the SERS mechanism for molecular vibrational modes, ERS signals also follow the fourth power of local field enhancement by plasmonic enhancement of both excitation and inelastic electronic scattering transitions.[3,4] Therefore, surface plasmon enhanced ERS signal intensity can be expressed as:

$$I_{\mathrm{ERS}}(\omega_o - \Delta\omega_e) = g_M(\omega_o)^2 \cdot g_M(\omega_o - \Delta\omega_e)^2 \cdot \sigma_{\mathrm{ERS}}(\omega_o, \Delta\omega_e) \cdot |n_{e-h}(\Delta\omega_e) + 1| \cdot A \cdot t \cdot I_o(\omega_o) \quad \text{(S1)}$$

where g_M is the average field-enhancement factor in the metal side of the hotspot, σ_{ERS} is the effective cross-section for the ERS process, A is the metal surface area of a unit-cell structure, t is the surface density of the individual nanostructures producing the enhancement and I_o is the intensity of incident laser. In terms of g_M, although integral over the entire hotspot should be conducted to acquire precise enhancement factor, we simplify g_M as the averaged enhancement factor since the electric field inside of the metal exponentially decays along the *z*-direction.[11,12] σ_{ERS} depends on the material property of the metal and consistent with the bulk material.[13] n_{e-h} is expressed as $|n_{e-h}(\Delta\omega_e) + 1|$ considering the overall thermodynamic factor for the Stokes-shifted ERS process.[2,14] While ERS signals show a continuous spectral feature because of the

continuous electronic *sp*-bands of the metal, molecular Raman scattering (MRS) signals carry many distinct narrow peaks in the measured spectra due to discrete inelastic energy shifts associated with discrete vibrational modes of a molecule (Figure 1B). Following the fourth power of local field enhancement, surface plasmon enhanced MRS signal intensity for a molecule placed in the plasmonic hotspot can be expressed as:

$$I_{\mathrm{MRS}}(\omega_o - \Delta\omega_m) = g_I(\omega_o)^2 \cdot g_I(\omega_o - \Delta\omega_m)^2 \cdot \sigma_{\mathrm{MRS}}(\omega_o, \Delta\omega_m) \cdot N \cdot r \cdot A \cdot t \cdot I_o(\omega_o) \quad \text{(S2)}$$

where g_I is the field-enhancement factor in the insulator side of the hotspot, σ_{MRS} is the cross-section for the MRS process, N is the concentration of the analyte molecules in hotspots, r is the effective coefficient related to the orientation of transition dipole moment for a specific vibrational mode of analyte molecules on a metallic surface (fixed or fluctuating). As both ERS and MRS signals originate from the same hotspots, the factors including A, t, $I_o(\omega_o)$ are no longer relevant. Therefore, we can express the ratio between I_{MRS} and I_{ERS} from the same hotspots as:

$$\frac{I_{\mathrm{MRS}}}{I_{\mathrm{ERS}}} = \frac{g_I(\omega_o)^2 \cdot g_I(\omega_o - \Delta\omega_m)^2 \cdot \sigma_{\mathrm{MRS}}(\omega_o, \Delta\omega_m) \cdot N \cdot r}{g_M(\omega_o)^2 \cdot g_M(\omega_o - \Delta\omega_e)^2 \cdot \sigma_{\mathrm{ERS}}(\omega_o, \Delta\omega_e) \cdot |n_{e-h}(\Delta\omega_e) + 1|} \quad \text{(S3)}$$

Since the electromagnetic boundary condition relates the dominant perpendicular electric fields at the metal-insulator interface at plasmonic hotspots, one can convert the terms of local field enhancement factors (g_M and g_I) into materials permittivity values at the metal-insulator interface based on the boundary condition. More specifically, we assume that the absorbed photons only induce a momentum change along with the *z*-direction, and thus only the *z*-component of the electric field contributes to the enhancement of the light absorption and emission with the continuous condition on the interface. Considering $g_I(\omega_o) \approx g_I(\omega_o - \Delta\omega_m)$ and $g_M(\omega_o) \approx$

$g_M(\omega_o - \Delta\omega_e)$ based on approximations of $\omega_o \approx \omega_o - \Delta\omega_m \gg \Delta\omega_m$ and $\omega_o \approx \omega_o - \Delta\omega_e \gg \Delta\omega_e$, the relation between near-field enhancement factors, g_I and g_M, can be expressed as:

$$\frac{g_I}{g_M} = \frac{E_{I-z}}{E_{M-z}} = \frac{\varepsilon_M}{\varepsilon_I}$$

where E_{I-z} and E_{M-z} are the normal components of the electric fields in the insulator and metal side, respectively, at the metal-dielectric interface, ε_M and ε_I are the complex permittivity of metal and insulator at ω_o, respectively. Thus, we can further simplify eq. (S3) as:

$$\frac{I_{\mathrm{MRS}}}{I_{\mathrm{ERS}}} = \left|\frac{\varepsilon_M}{\varepsilon_I}\right|^4 \frac{\sigma_{\mathrm{MRS}}(\omega_o, \Delta\omega_m)}{\sigma_{\mathrm{ERS}}(\omega_o, \Delta\omega_e)} \frac{1}{|n_{e-h}(\Delta\omega_e)+1|} \cdot r \cdot N = C \cdot r \cdot N \quad \text{(S4)}$$

For typical SERS measurements under a CW excitation laser at room temperature, excluding r and N, all other terms in eq. (S4) can be grouped into a material-related parameter C, where $C = \left|\frac{\varepsilon_M}{\varepsilon_I}\right|^4 \frac{\sigma_{\mathrm{MRS}}(\omega_o, \Delta\omega_m)}{\sigma_{\mathrm{ERS}}(\omega_o, \Delta\omega_e)} \frac{1}{|n_{e-h}(\Delta\omega_e)+1|}$. C does not depend on the incident laser intensity $I_o(\omega_o)$ as well as local field enhancement factors (g_I and g_M) at hotspots. Therefore, the ERS-calibrated MRS signals $I_{\mathrm{MRS}}/I_{\mathrm{ERS}}$ can be insensitive to variations of SERS EFs between different hotspots and thus can better quantify the concentration of analyte molecules (or more accurately, the density of molecular vibrational modes) compared to the directly measured I_{MRS} at hotspots on SERS substrates.

Fabrication of nanolaminate SERS substrates

Detailed fabrication steps are described elsewhere.[15] First, a composite polydimethylsiloxane (PDMS) stamp having a diameter of 120 nm, a period of 400 nm, and a height of 150 nm, was prepared from a silicon wafer patterned with nanopillar structures by soft lithography.[16] With the PDMS stamp, UV-curable polyurethane (PU) was used to fabricate a periodic nanopillar array by

molding on a flexible and optically transparent polyester film. After UV curing for 10 min, an additional heat-curing process was performed in a convection oven at 80 ℃ overnight. Next, we deposited alternating layers of Au and SiO_2 by electron-beam evaporation. The four Au layers have the same thickness of 30 nm, and the thicknesses of three SiO_2 layers are nominally 6 nm, 8 nm, and 12 nm from bottom to top. Also, we deposited 1 nm of Cr between polymer nanopillar array and the first layer of Au, and 0.7 nm thick Ti between metal and insulator layers as adhesion layers.

Experimental setup

A confocal Raman microscope equipped with a 785 nm diode laser was used for SERS measurements. Before the measurement, the instrumental calibration was verified by the silicon peak at 520 cm^{-1}. All measurements were conducted in the backscattering geometric configuration at room temperature. Elastically scattered radiation at the wavelength corresponding to the laser line (Rayleigh scattering) is filtered out by a long pass filter, while the rest of the collected light was guided through a multimode fiber (100 μm core diameter), acting as the pinhole for a confocal microscope, to a spectrometer. The backscattered photons were dispersed with a 300 groove/mm (750 nm blaze grating) and detected by a CCD camera, which was thermoelectrically cooled and maintained at -60 °C. For benzenethiol (BZT) experiments, ethanol-based 1 mmol/L BZT solution was prepared, and samples were incubated for overnight, followed by ethanol rinsing. For Rhodamine 6G (R6G) measurements, phosphate-buffered saline (PBS)-based R6G solutions with different concentrations were prepared. During the measurements, the samples were immersed in the solutions.

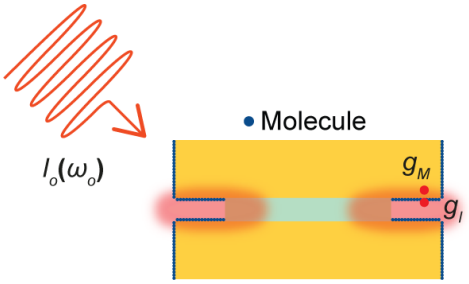

Figure S1. Schematic illustration of a single unit cell of the nanolaminate SERS substrates.

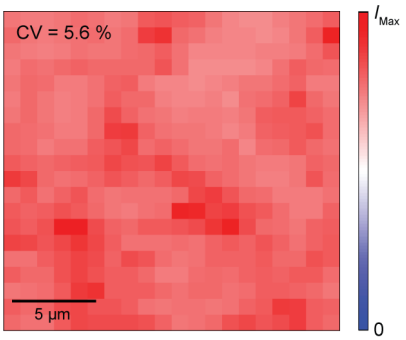

Figure S2. 2D Raman mapping of BZT on the nanolaminate SERS substrate without sample buckling.

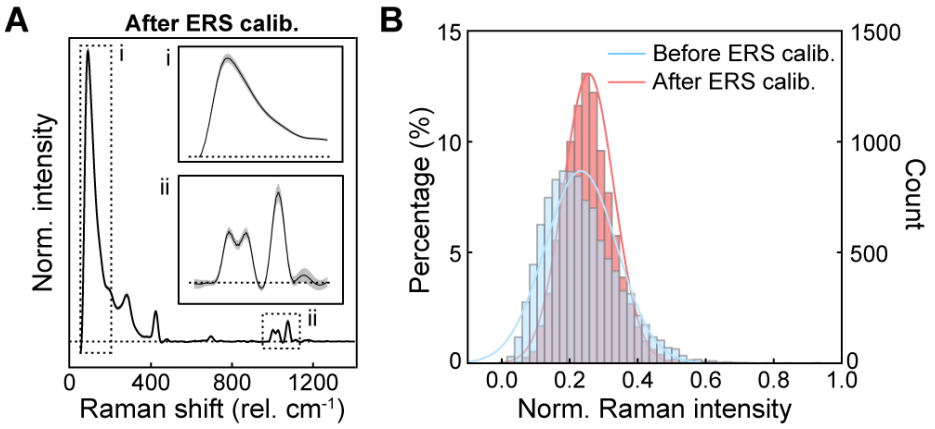

Figure S3. (A) Average BZT SERS spectrum with one SD (gray regions) from 10,000 pixels after ERS calibration. (B) Histograms of BZT SERS signal intensities before and after ERS calibration.

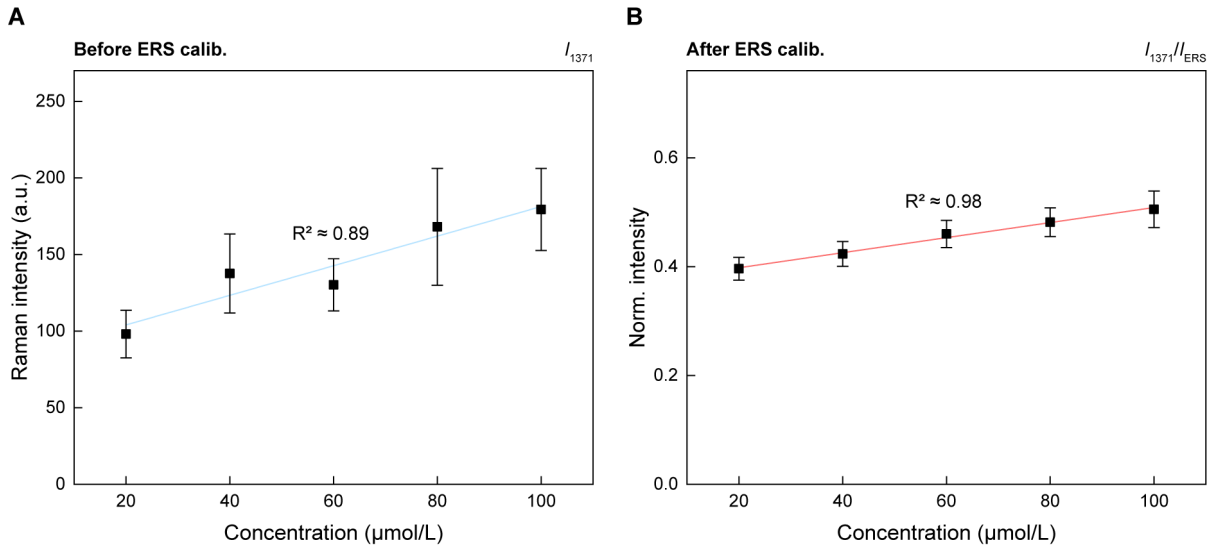

Figure S4. Working curves of solution-based R6G molecules with different concentrations from 20 μmol/L to 100 μmol/L using 1371 cm^{-1} (A) before and (B) after ERS calibration. The error bars show one standard deviation from 400 pixels.

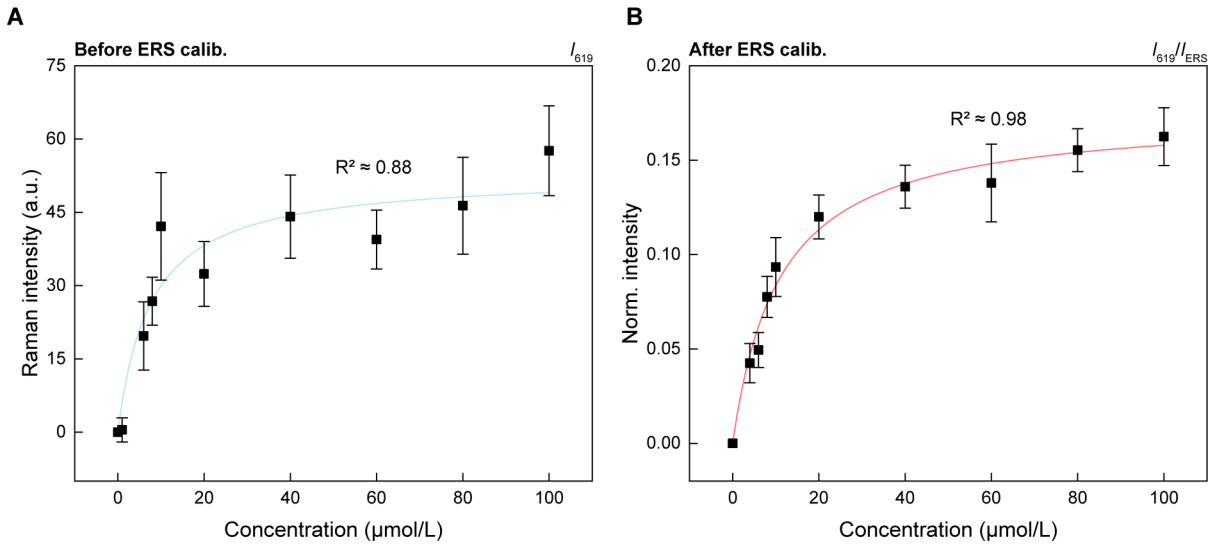

Figure S5. Working curves of solution-based R6G molecules with different concentrations from 4 μmol/L to 100 μmol/L using 619 cm^{-1} (A) before and (B) after ERS calibration. The error bars show one standard deviation from 400 pixels.

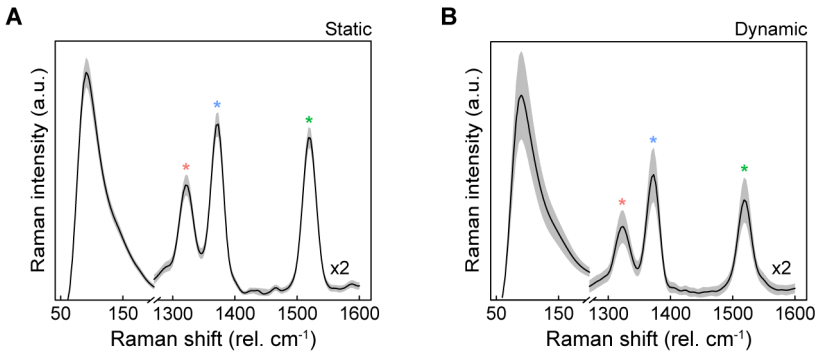

Figure S6. Temporally averaged Raman spectra with one SD (gray regions) from single-spot time-resolved SERS measurements over 300 s under (A) static and (B) dynamic laser excitation. Intensities in the MRS region between 1300 cm^{-1} and 1600 cm^{-1} are multiplied by two for clarity.

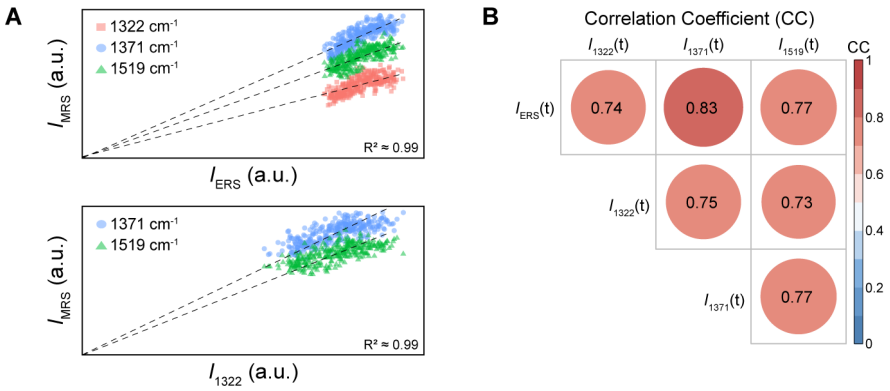

Figure S7. (A) The scatter plots of I_{MRS} as a function of I_{ERS} (top) and I_{1322} (bottom) under static laser excitation. (B) A matrix of calculated correlation coefficients among ERS and MRS signals under static laser excitation.

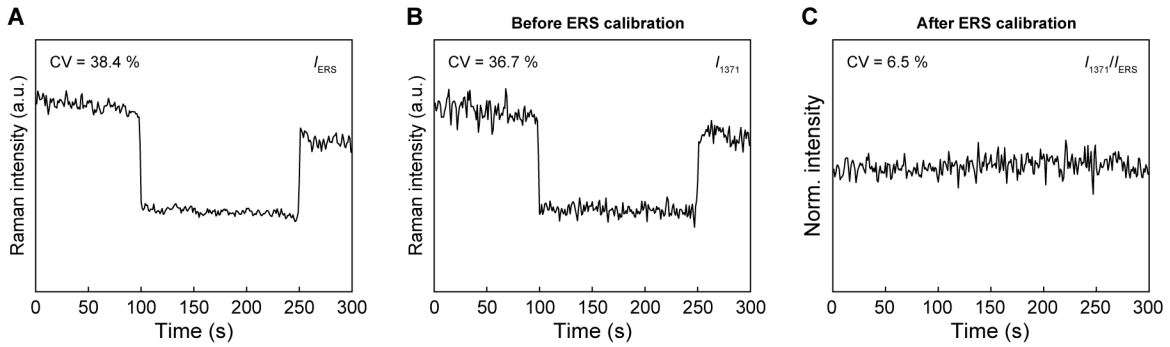

Figure S8. Time-trajectories of (A) ERS and MRS signals using 1371 cm^{-1} (B) before and (C) after ERS calibration with abrupt laser power changes between 0.25 mW and 0.5 mW.

References

1. Ashcroft, N.; Mermin, N. *New York* **1976**.
2. Carles, R.; Bayle, M.; Benzo, P.; Benassayag, G.; Bonafos, C.; Cacciato, G.; Privitera, V. *Physical Review B* **2015,** 92, (17).
3. Hugall, J. T.; Baumberg, J. J. *Nano Lett* **2015,** 15, (4), 2600-4.
4. Mertens, J.; Kleemann, M. E.; Chikkaraddy, R.; Narang, P.; Baumberg, J. J. *Nano Lett* **2017,** 17, (4), 2568-2574.
5. Huang, J.; Wang, W.; Murphy, C. J.; Cahill, D. G. *Proc Natl Acad Sci U S A* **2014,** 111, (3), 906-11.
6. Brandt, N. C.; Keller, E. L.; Frontiera, R. R. *J Phys Chem Lett* **2016,** 7, (16), 3179-85.
7. Roloff, L.; Klemm, P.; Gronwald, I.; Huber, R.; Lupton, J. M.; Bange, S. *Nano Lett* **2017,** 17, (12), 7914-7919.
8. Saavedra, J. R. M.; Asenjo-Garcia, A.; de Abajo, F. J. G. *Acs Photonics* **2016,** 3, (9), 1637-1646.
9. Haug, T.; Klemm, P.; Bange, S.; Lupton, J. M. *Phys Rev Lett* **2015,** 115, (6), 067403.
10. Lin, K.-Q.; Yi, J.; Hu, S.; Sun, J.-J.; Zheng, J.-T.; Wang, X.; Ren, B. *ACS Photonics* **2016,** 3, (7), 1248-1255.
11. Sigle, D. O.; Mertens, J.; Herrmann, L. O.; Bowman, R. W.; Ithurria, S.; Dubertret, B.; Shi, Y. M.; Yang, H. Y.; Tserkezis, C.; Aizpurua, J.; Baumberg, J. J. *Acs Nano* **2015,** 9, (1), 825-830.
12. Tserkezis, C.; Esteban, R.; Sigle, D. O.; Mertens, J.; Herrmann, L. O.; Baumberg, J. J.; Aizpurua, J. *Phys Rev A* **2015,** 92, (5).
13. Lin, K. Q.; Yi, J.; Zhong, J. H.; Hu, S.; Liu, B. J.; Liu, J. Y.; Zong, C.; Lei, Z. C.; Wang, X.; Aizpurua, J.; Esteban, R.; Ren, B. *Nat Commun* **2017,** 8, 14891.
14. Mahajan, S.; Cole, R. M.; Speed, J. D.; Pelfrey, S. H.; Russell, A. E.; Bartlett, P. N.; Barnett, S. M.; Baumberg, J. J. *J Phys Chem C* **2010,** 114, (16), 7242-7250.
15. Nam, W.; Ren, X.; Tali, S. A. S.; Ghassemi, P.; Kim, I.; Agah, M.; Zhou, W. *Nano Lett* **2019,** 19, (10), 7273-7281.
16. Qin, D.; Xia, Y.; Whitesides, G. M. *Nat Protoc* **2010,** 5, (3), 491-502.